

# NiO/CNTs derived from metal-organic frameworks as superior anode material for lithium-ion batteries

Yingqiao Xu<sup>1</sup> · Shujin Hou<sup>1</sup> · Guang Yang<sup>1</sup> · Ting Lu<sup>1</sup> · Likun Pan<sup>1</sup>

Received: 25 July 2017 / Revised: 11 October 2017 / Accepted: 14 October 2017 / Published online: 26 October 2017  
© Springer-Verlag GmbH Germany 2017

**Abstract** In this work, porous NiO microspheres interconnected by carbon nanotubes (NiO/CNTs) were successfully fabricated by the pyrolysis of nickel metal-organic framework precursors with CNTs and evaluated as anode materials for lithium-ion batteries (LIBs). The structures, morphologies, and electrochemical performances of the samples were characterized by X-ray diffraction, N<sub>2</sub> adsorption-desorption, field emission scanning electron microscopy, cyclic voltammetry, galvanostatic charge/discharge tests, and electrochemical impedance spectroscopy, respectively. The results show that the introduction of CNTs can improve the lithium-ion storage performance of NiO/CNT composites. Especially, NiO/CNTs-10 exhibits the highest reversible capacity of 812 mAh g<sup>-1</sup> at 100 mA g<sup>-1</sup> after 100 cycles. Even cycled at 2 A g<sup>-1</sup>, it still maintains a stable capacity of 502 mAh g<sup>-1</sup> after 300 cycles. The excellent electrochemical performance of NiO/CNT composites should be attributed to the formation of 3D conductive network structure with porous NiO microspheres linked by CNTs, which benefits the electron transfer ability and the buffering of the volume expansion during the cycling process.

**Keywords** Metal-organic frameworks · NiO/CNTs · Anode materials · Lithium-ion batteries · 3D conductive network structure

**Electronic supplementary material** The online version of this article (<https://doi.org/10.1007/s10008-017-3811-0>) contains supplementary material, which is available to authorized users.

✉ Ting Lu  
tlu@phy.ecnu.edu.cn

<sup>1</sup> Shanghai Key Laboratory of Magnetic Resonance, School of Physics and Materials, East China Normal University, 3663 N. Zhongshan Rd., Shanghai 200062, China

## Introduction

Lithium-ion batteries (LIBs) have been widely used as power sources in consumer electronics such as cellular phones, laptops, and full and hybrid electric vehicles due to their long cycling life, high energy capacity, and environmental friendliness [1–3]. However, the current commercial graphite exhibits the limited theoretical capacity of 372 mAh g<sup>-1</sup>, which cannot meet the increasing demand of LIBs [4, 5]. Therefore, substantial efforts have been developed to explore suitable electrode materials for LIBs with high capacity and long cycle life.

Recently, fabrication of various nanostructured transition metal oxides (TMOs), such as nanorods [6], nanoflowers [7], nanosheets [8], and urchins [9], has been developed for excellent anode materials owing to their higher theoretical capacities and energy densities compared to graphite. The motivated construction not only effectively accommodates the volume change during cycling process, but also improves the lithium-ion diffusion and storage performance [10, 11]. Many methods have been explored to synthesize nanostructured TMOs over the last few decades. Thereinto, metal-organic frameworks (MOFs), a class of crystallized polymeric porous materials consisting of metal ions or clusters with organic bridging ligands [12, 13], have been served as the effective precursors to form nanostructured TMOs by thermal decomposition [14, 15]. The TMOs derived from MOFs always reveal satisfied performance and have been widely applied in catalysis [16, 17], biomedicine [18], supercapacitors [19, 20], LIBs [21, 22], etc., due to their hierarchical structures and high surface areas. Among various TMOs for LIBs, NiO has attracted much attention because of its high theoretical capacity (718 mAh g<sup>-1</sup>), low cost, environmental benignity, and abundance [23–25]. For example, porous NiO was fabricated by solid-state thermolysis of Ni-MOF for LIBs

and exhibited a high initial capacity of  $\sim 800 \text{ mAh g}^{-1}$  at  $100 \text{ mA g}^{-1}$  [26]. Mollamahale et al. reported that NiO nanoflowers used as anodes for LIBs displayed a reversible capacity of  $551.8 \text{ mAh g}^{-1}$  at a current density of  $100 \text{ mA g}^{-1}$  after 50 cycles [7]. Unfortunately, poor rate behavior and fast capacity fading are the main obstacles for the commercialization of TMOs for LIBs, which are mainly caused by the poor electrical conductivity and huge volume change during lithiation/delithiation cycles [27, 28].

For this, one effective strategy used to improve the aforementioned problems is to introduce carbonaceous materials into TMOs for increasing the electrical conductivity and the structural stability [29–31]. Among various carbon materials, carbon nanotubes (CNTs) are characterized as 1D tubular structure with excellent electrical conductivity and chemical stability [32, 33]. Porous  $\text{Co}_3\text{O}_4/\text{CNT}$  composites were synthesized via the decomposition of ZIF-67/CNTs and showed an excellent specific capacity of  $813 \text{ mAh g}^{-1}$  at a current density of  $100 \text{ mA g}^{-1}$  after 100 cycles, while that of pure  $\text{Co}_3\text{O}_4$  was only  $118 \text{ mAh g}^{-1}$  [34]. Porous ZnO/CNT composites obtained from Zn-MOFs/CNT precursors exhibited superior lithium-ion storage performance with a high reversible capacity of  $419.8 \text{ mAh g}^{-1}$  after 100 cycles at  $200 \text{ mA g}^{-1}$ , while the pure ZnO sample was eventually stabilized with a capacity of less than  $200 \text{ mAh g}^{-1}$  [35]. Above all, introducing 1D CNTs into MOF-based NiO should be an effective way to enhance the lithium-ion transport and storage performance for LIBs.

In this work, MOF-based NiO/CNT composites were fabricated by a facile hydrothermal method and subsequent thermal treatment, in which CNTs are embedded in porous NiO microspheres and connect them to form a 3D network structure. Moreover, NiO microspheres are assembled by nanoparticles, leading to the formation of abundant effective channels for ion migration. As expected, an excellent lithium-ion storage performance with remarkable cycling stability and good rate capability is obtained.

## Experimental section

### Material synthesis

Firstly, CNTs were pre-treated by a mixture of nitric acid and sulfuric acid (3:1), which has been described in previous report [36]. In a typical synthesis, 864 mg  $\text{Ni}(\text{NO}_3)_2 \cdot 6\text{H}_2\text{O}$ , 3 g PVP (K-30), and a certain amount of pre-treated CNTs were dissolved in 60 mL mixed solution (DMF/distilled water/ethanol = 1:1:1 v/v/v) to obtain a well-dispersed suspension by ultrasonication for 1 h, followed by adding 300 mg benzene-1,3,5-tricarboxylic acid ( $\text{H}_3\text{BTC}$ ). Then, the solution

was stirred for 3 h at room temperature to form a black solution. Subsequently, the mixture was sealed into a Teflon-lined autoclave and heated at  $150 \text{ }^\circ\text{C}$  for 10 h. After that, the solid product was collected by centrifugation, washed with DMF and ethanol for several times, and dried at  $80 \text{ }^\circ\text{C}$  for 12 h. The as-synthesized Ni-MOF/CNTs was heated to  $450 \text{ }^\circ\text{C}$  at a rate of  $2 \text{ }^\circ\text{C min}^{-1}$  and kept for 30 min under nitrogen gas flow. After that, the resulting black powders were treated at  $350 \text{ }^\circ\text{C}$  in air for 30 min with a rate of  $1 \text{ }^\circ\text{C min}^{-1}$  to obtain the NiO/CNT composites. The composites with different amount of CNTs (CNTs/Ni-MOF = 5:100, 10:100, 20:100) were labeled as NiO/CNT-5, NiO/CNT-10, and NiO/CNT-20, respectively. For comparison, pure NiO was synthesized through a similar process without the addition of CNTs.

### Characterization

The crystalline structure of the samples was tested using an X-ray diffraction (XRD) patterns with Cu-K $\alpha$  radiation ( $\lambda = 0.154 \text{ nm}$ ). The microstructures and morphologies of the samples were observed by field emission scanning electron microscopy (FESEM, Hitachi S-4800) equipped with a Bruker QUANTAX-400 energy-dispersive spectrometry (EDS). Thermogravimetric analysis (TGA) was performed to analyze the carbon content in the composites using a Shimadzu-50 thermoanalyzer in air with a heating rate of  $10 \text{ }^\circ\text{C min}^{-1}$  from room temperature to  $800 \text{ }^\circ\text{C}$ .  $\text{N}_2$  adsorption/desorption isotherms were measured at 77 K using an ASAP 2020 Accelerated Surface Area and Porosimetry System (Micromeritics, Norcross, GA) based on Brunauer-Emmett-Teller (BET) multipoint method, and the pore size distributions were obtained from the adsorption branches using Barrett-Joyner-Halenda (BJH) model.

### Electrochemical experiments

Electrochemical performances of the products were evaluated as anode materials of LIBs in 2032-type coin cells, using pure lithium foil as the counter and reference electrode, Whatman glass fiber membrane as separator, and 1 M  $\text{LiPF}_6$  dissolved in dimethyl carbonate, ethylene carbonate, and ethyl methyl carbonate (with a weight ratio of 1:1:1) as the electrolyte. Homogenous slurry mixed by the as-prepared samples, Super-P, and carboxymethyl cellulose (80:10:10 w/w/w) in deionized water was coated on a copper foil and dried in a vacuum oven at  $120 \text{ }^\circ\text{C}$  for 24 h as the test electrode. Cycling performances were tested in a range of 0.005–3 V by the Land 2001A battery test system. Cyclic voltammetry (CV) was carried out by an electrochemical workstation (AUTOLAB PGSTA302N) in a voltage range of 0.005–3 V at room temperature. After 100 cycles, the electrochemical impedance spectroscopy (EIS) measurements were conducted on the same electrochemical workstation in a frequency range of

0.1–100 kHz, and applied bias voltage and ac amplitude were set at the open circuit voltage of the cells and 5 mV, respectively.

## Results and discussion

The facile and scalable strategy for synthesizing NiO/CNTs is displayed in Scheme 1.  $\text{Ni}(\text{NO}_3)_2 \cdot 6\text{H}_2\text{O}$  and  $\text{H}_3\text{BTC}$  were used as metal source and organic ligand, respectively. Firstly, the CNT surface was functionalized with electronegative carboxyl groups by acid treatment, which is beneficial for loading  $\text{Ni}^{2+}$  by electrostatic interaction in the reaction solution. Subsequently, the PVP, served as the stabilizing agent to form a spherical structure [37], was added for the formation of Ni-MOF on the surface of CNTs [38]. After a hydrothermal method, CNTs were embedded in the Ni-MOFs microspheres to form a 3D conductive network. Finally, the NiO/CNTs were obtained from Ni-MOFs/CNTs by a simple annealing treatment.

The crystal structures of the as-prepared samples were characterized by XRD measurement, as shown in Fig. 1. The peaks of pure NiO at  $37.2^\circ$ ,  $43.05^\circ$ ,  $62.69^\circ$ ,  $75.3^\circ$ , and  $79.2^\circ$  are indexed to (111), (200), (220), (311), and (222) planes of cubic NiO (JPCDS card No. 47-1049), and no other impurity peaks are found, indicating the high purity of the products [39]. After the introduction of CNTs, a new characteristic peak at around  $25.7^\circ$  appears for all the NiO/CNTs and its intensity increases with the increase of CNT content, which corresponds to the typical (002) facet of the graphitic carbon [40]. At the meantime, the main diffraction peaks of all the NiO/CNT composites are similar to those of pure NiO, indicating that the existence of CNTs does not result in the new crystal orientations or changes in preferential orientations of NiO. The calculated cell parameters and volume are shown in Table S1. A careful observation shows that there is no obvious shift occurring for the diffraction peak (111) of NiO and the cell parameters of different composites are similar

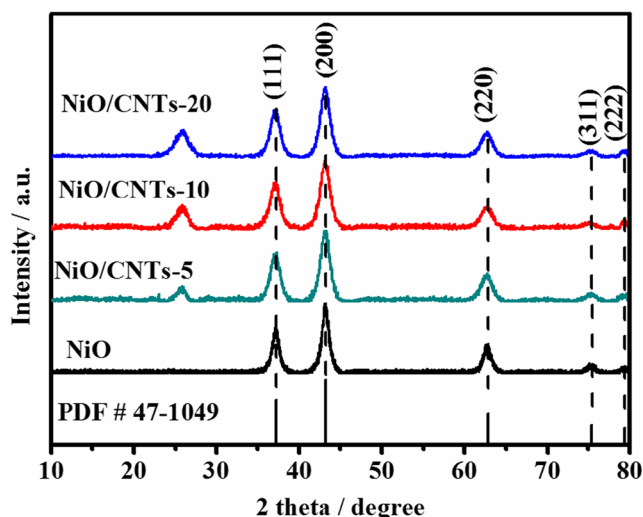
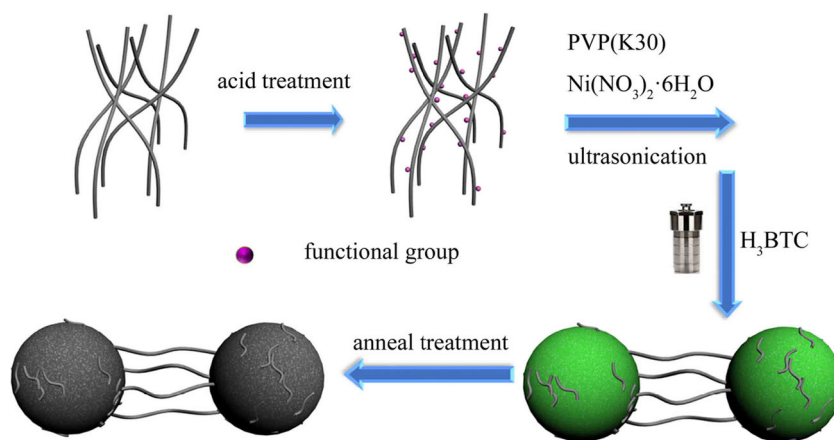


Fig. 1 XRD patterns of NiO/CNTs and NiO

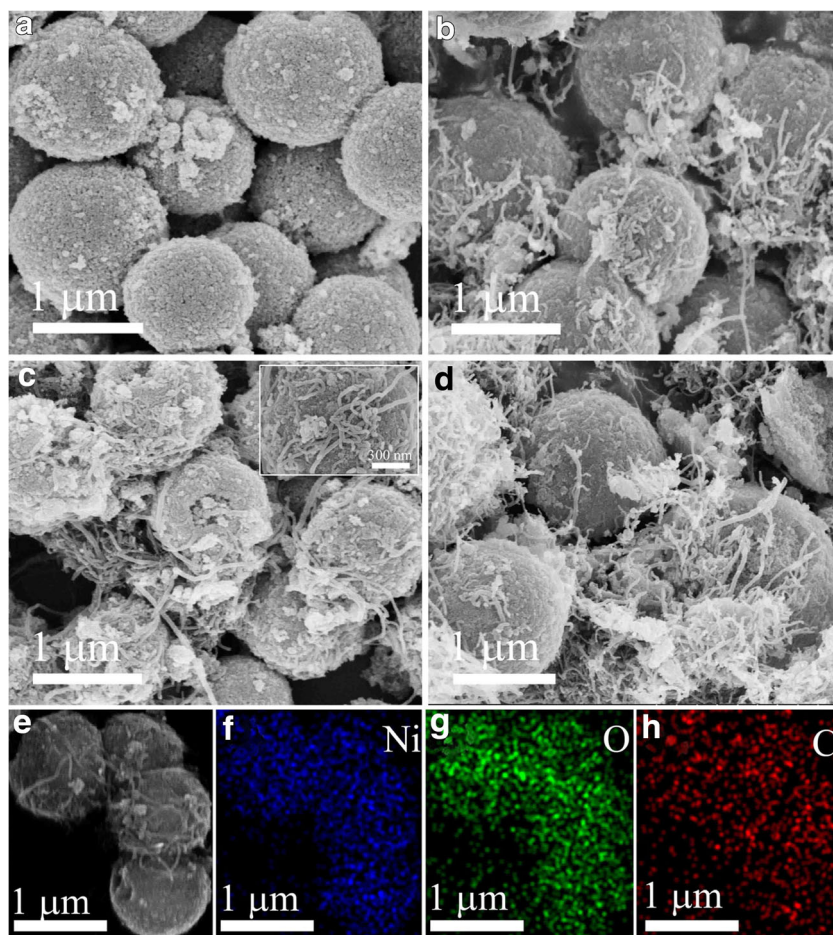
( $4.1748$ ,  $4.1754$ ,  $4.1753$ , and  $4.1753$  Å for NiO, NiO/CNTs-5, NiO/CNTs-10, and NiO/CNTs-20) after the introduction of CNTs. The slight difference of the aforementioned cell parameters was ascribed to the uncertainties in the refinement rather than an actual change in size [41].

To further investigate the morphologies and structures of NiO and NiO/CNTs, FESEM measure was carried out, as shown in Fig. 2a–d. It can be clearly observed that NiO (Fig. 2a) derived from Ni-MOFs displays microsphere structure (diameter  $1\sim 1.5$  μm) with rough surface consisting of small nanoparticles, which results in abundant internal pores for a good electrolyte infiltration. As shown in Fig. 2b, c, after the introduction of the CNTs, the NiO microspheres are connected by CNTs to form a 3D conductive network structure. Obviously, it can be seen from the inset in Fig. 2c that the CNTs are embedded in the NiO microspheres, which would favor the fast lithium-ion transportation and improve the structure stability during cycling process. In addition, it can be further observed from Fig. S1 that CNTs are not only present on the surface of the NiO microspheres

Scheme 1 Schematic illustration of the formation of NiO/CNTs



**Fig. 2** FESEM images of NiO (a), NiO/CNTs-5 (b), NiO/CNTs-10 (c) (inset shows the high-magnification image), NiO/CNTs-20 (d), and elemental mapping images of NiO/CNTs-10 (e–h)



but also embedded in the NiO microspheres. However, when the content of CNTs further increases (Fig. 2d), the excessive CNTs agglomerate together easily and block the porous conductive network. The elemental mapping (Fig. 2e–h) measurement confirms that Ni, O, and C elements are uniformly distributed in the NiO/CNTs, indicating the good contact between NiO and CNTs. The mapping images of NiO are also displayed in Fig. S2. It is clearly seen that the Ni and O elements are uniformly distributed throughout the structure.

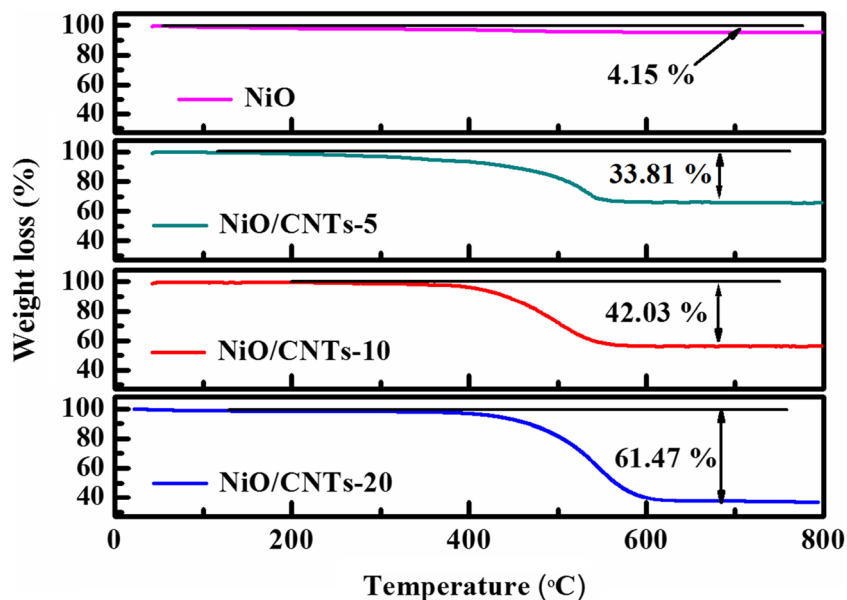
TGA measurement in air was employed to identify the carbon content in the as-prepared composites, and the corresponding curve is shown in Fig. 3. During the thermal treatment in air, the huge weight loss observed from 350 to 550 °C could be attributed to the decomposition of organic ligands [34], while CNTs are still stable [42]. The real CNT contents in NiO/CNTs-5, NiO/CNTs-10, and NiO/CNTs-20 are about 29.66, 37.88, and 57.32 wt%, respectively.

The specific surface areas and pore size distributions of NiO, NiO/CNTs-5, NiO/CNTs-10, and NiO/CNTs-20 were investigated by N<sub>2</sub> adsorption and desorption isotherms, as shown in Fig. 4a. Obviously, both of samples show a typical IV type with a hysteresis loop in the pressure range of  $0.8 < P/P_0 < 0.99$ , demonstrating the existence of mesoporous

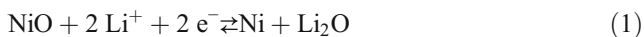
structure [20, 43]. The BET surface area and the total pore volume of NiO/CNTs-10 are  $134.68 \text{ m}^2 \text{ g}^{-1}$  and  $0.75 \text{ cm}^3$ , much larger than those of NiO ( $82.66 \text{ m}^2 \text{ g}^{-1}$ ,  $0.424 \text{ cm}^3$ ), NiO/CNTs-5 ( $87.94 \text{ m}^2 \text{ g}^{-1}$ ,  $0.476 \text{ cm}^3$ ), and NiO/CNTs-20 ( $128.59 \text{ m}^2 \text{ g}^{-1}$ ,  $0.676 \text{ cm}^3$ ), which should promote the intercalation and diffusion of lithium-ion [44]. From the pore size distribution profiles (Fig. 4b), it can be indicated that all samples possess a mesoporous structure with a main pore distribution in the range of 2–40 nm, which benefits the buffering of large volume expansion of NiO during lithium insertion/extraction cycling [45]. It should be mentioned that the increase of BET surface area with the increase of CNT content (29.66–37.88 wt%) is ascribed to the formation of network structure, while the BET surface area decreases as the CNT content is further increased to 57.32 wt%, resulting in their agglomeration, which is consistent with the FESEM image of NiO/CNTs-20 (Fig. 2d).

As shown in Fig. 5a, b, the electrochemical performances of the NiO and NiO/CNTs-10 composites were investigated by CV curves within a voltage range of 0.005–3 V at a scan rate of  $0.2 \text{ mV s}^{-1}$ . For NiO (Fig. 5a), in the first cathodic process, there are two obvious peaks at about 0.25 and 0.7 V, which correspond to the formation of solid electrolyte

**Fig. 3** TGA curves of NiO, NiO/CNTs-5, NiO/CNTs-10, and NiO/CNTs-20 at a ramping rate of 10 °C min<sup>-1</sup> from room temperature to 800 °C



interphase (SEI) films resulting from the decomposition of electrolyte and the reduction of Ni<sup>2+</sup> to metallic Ni, respectively [45, 46]. However, in the subsequent cycles, the reduction peak shifts to around 0.91 V, which agrees well with the result reported previously [47]. In the anodic scans, there are two peaks at approximately 1.6 and 2.25 V, which are assigned to the partial decomposition of SEI films and the conversion of Ni to NiO, respectively [48, 49]. The electrochemical reaction in cycling process can be described as follows:



It can be found that the CV curves of NiO/CNTs-10 (Fig. 5b) display a similar trend to those of NiO. In the first cycle, the

peak is located at 0.33 V, which originates mainly from the formation of SEI layer [45]. Another peak at 0.91 V can be ascribed to the reduction of Ni<sup>2+</sup> to Ni, which is different from that of NiO (0.7 V) and mainly caused by the synergistic effect of both NiO and CNTs during lithiation/delithiation cycles [36].

Furthermore, Fig. 5c, d displays the 1st, 2nd, 5th, 10th, and 20th charge-discharge curves of the NiO and NiO/CNTs-10 electrodes at a current density of 100 mA g<sup>-1</sup>. It can be found that both of the electrodes deliver a large irreversible capacity in the first cycle, which is ascribed to the formation of SEI films due to the decomposition of the electrolyte [24, 48]. This phenomenon is common for transition metal oxides anode materials [32, 50]. After the first cycle, both of them display a long flat discharge potential plateau at about 0.9 V, which is

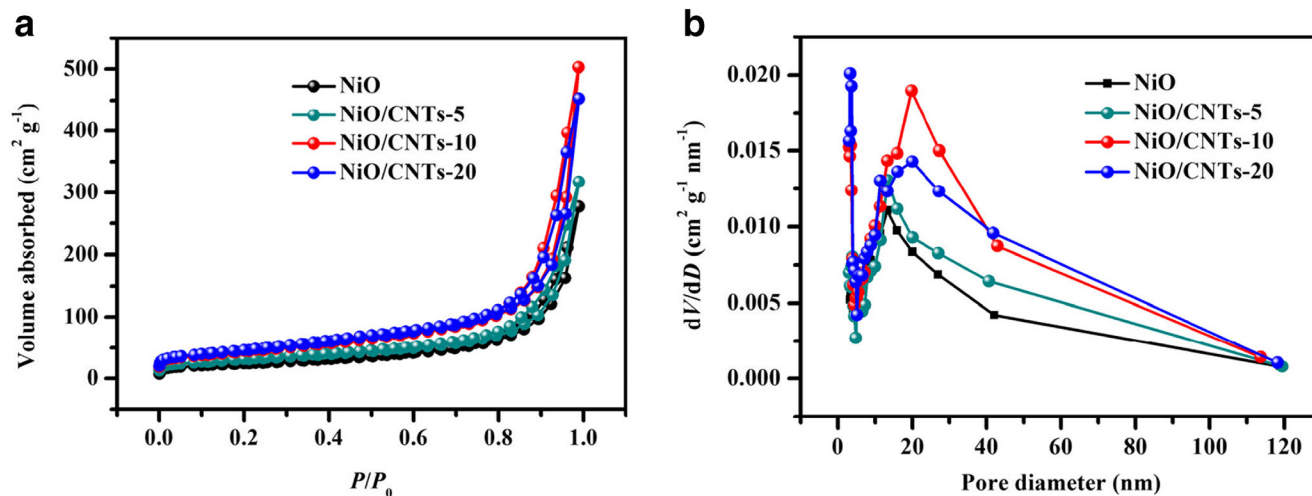


**Fig. 4** a Nitrogen adsorption/desorption isotherms and b pore size distribution of NiO, NiO/CNTs-5, NiO/CNTs-10, and NiO/CNTs-20

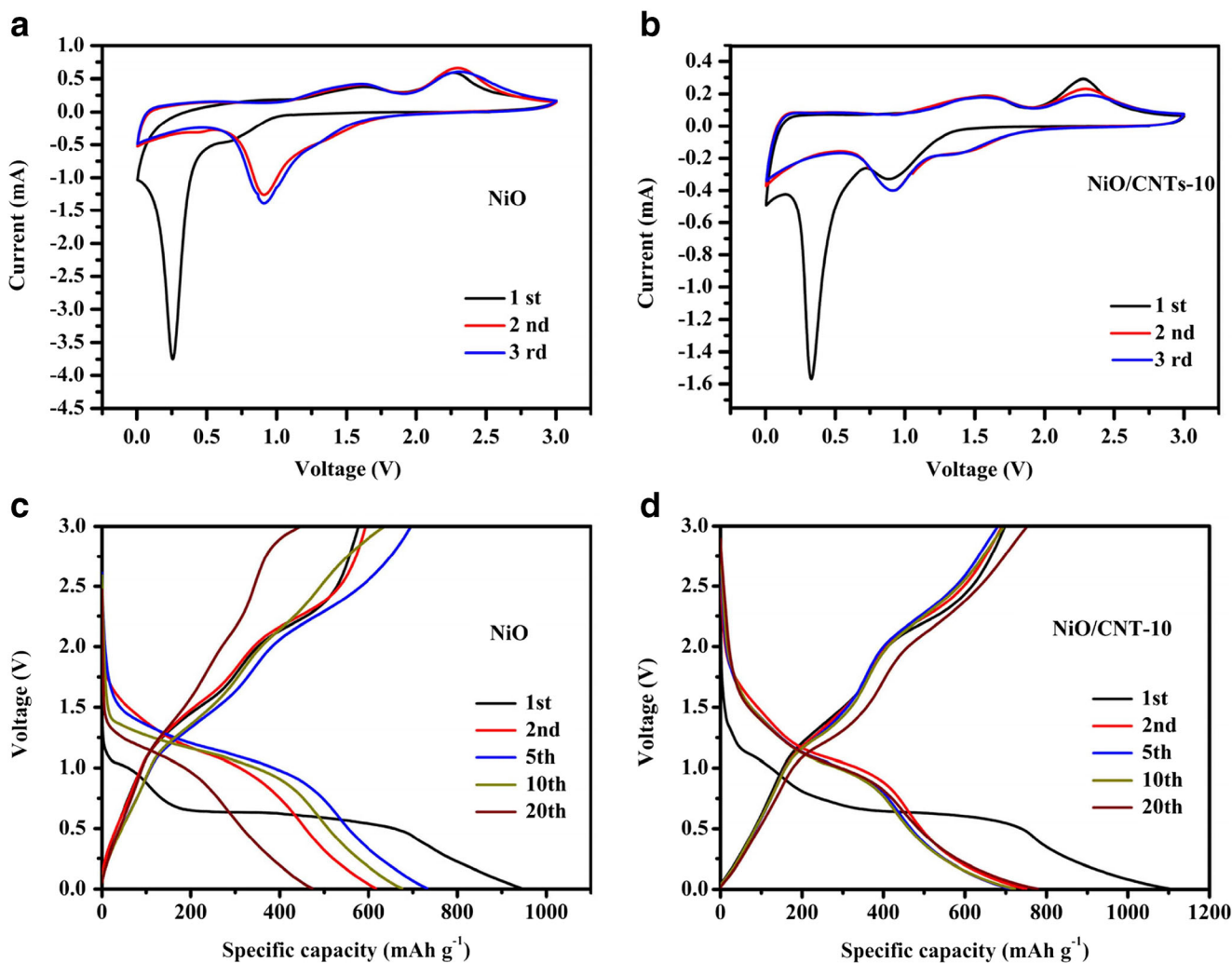


**Fig. 5** CV curves of **a** NiO and **b** NiO/CNTs-10. Charge-discharge profiles of **c** NiO and **d** NiO/CNTs-10 at a current density of  $100 \text{ mA g}^{-1}$

consistent with the CV measurement results. The NiO electrode exhibits a high initial discharge capacity of  $944.2 \text{ mAh g}^{-1}$  while much higher capacity of  $1100 \text{ mAh g}^{-1}$  is achieved for NiO/CNT-10. Moreover, the charge/discharge curves of NiO/CNTs-10 almost overlap from the second cycle, indicating a good cycling stability and electrochemical reversibility.

The EIS spectra of the NiO and NiO/CNT composite electrodes were recorded after 100 cycles at the current density of  $100 \text{ mA g}^{-1}$ , as shown in Fig. 6a. The Nyquist plots can be fitted with an equivalent electric circuit model, as shown in the inset of Fig. 6a.  $R_f$  in the high frequency region is ascribed to the SEI layer. The large semicircle in the middle frequency region is related to charge transfer resistance ( $R_{ct}$ ) and the straight line in the low frequency region represents the Warburg impedance of lithium-ion diffusion [40]. The  $R_{ct}$  values of NiO, NiO/CNTs-5, NiO/CNTs-10, and NiO/CNTs-20 are 386.9, 315.2, 66.09, and  $117.7 \Omega$ , implying that the  $R_{ct}$  of NiO is remarkably improved after introducing CNTs by the synergistic effect between imbedded CNTs and porous NiO microspheres. However, when the content of CNTs increases

(NiO/CNTs-20), the value of  $R_{ct}$  increases, which should be caused by the agglomeration of the excessive CNTs with poor electrochemical activity (Fig. 2d), as observed in FESEM image, resulting in unsatisfied kinetic performance of the electrode [51].

Figure 6b shows the rate performance of NiO/CNT-10 at various current densities from  $0.1$  to  $4 \text{ A g}^{-1}$ . When the current density increases from  $0.1$  to  $4 \text{ A g}^{-1}$ , the NiO/CNT-10 electrode delivers average reversible capacities of 885.51, 851.20, 838.44, 777.58, 479.76, and  $232.56 \text{ mAh g}^{-1}$ , respectively. What's more, when the current density returns back to  $0.1 \text{ A g}^{-1}$ , the specific capacity can be recovered to about  $849.4 \text{ mAh g}^{-1}$ . The excellent rate performance can be ascribed to the improvement of the lithium-ion diffusion capability and excellent structural stability at different rate values.

Figure 6c displays the cycling performances of the NiO and NiO/CNT electrodes at a current density of  $100 \text{ mA g}^{-1}$  for 100 cycles. The specific capacity of pure NiO electrode drops from  $948 \text{ mAh g}^{-1}$  at first cycle to  $122 \text{ mAh g}^{-1}$  after

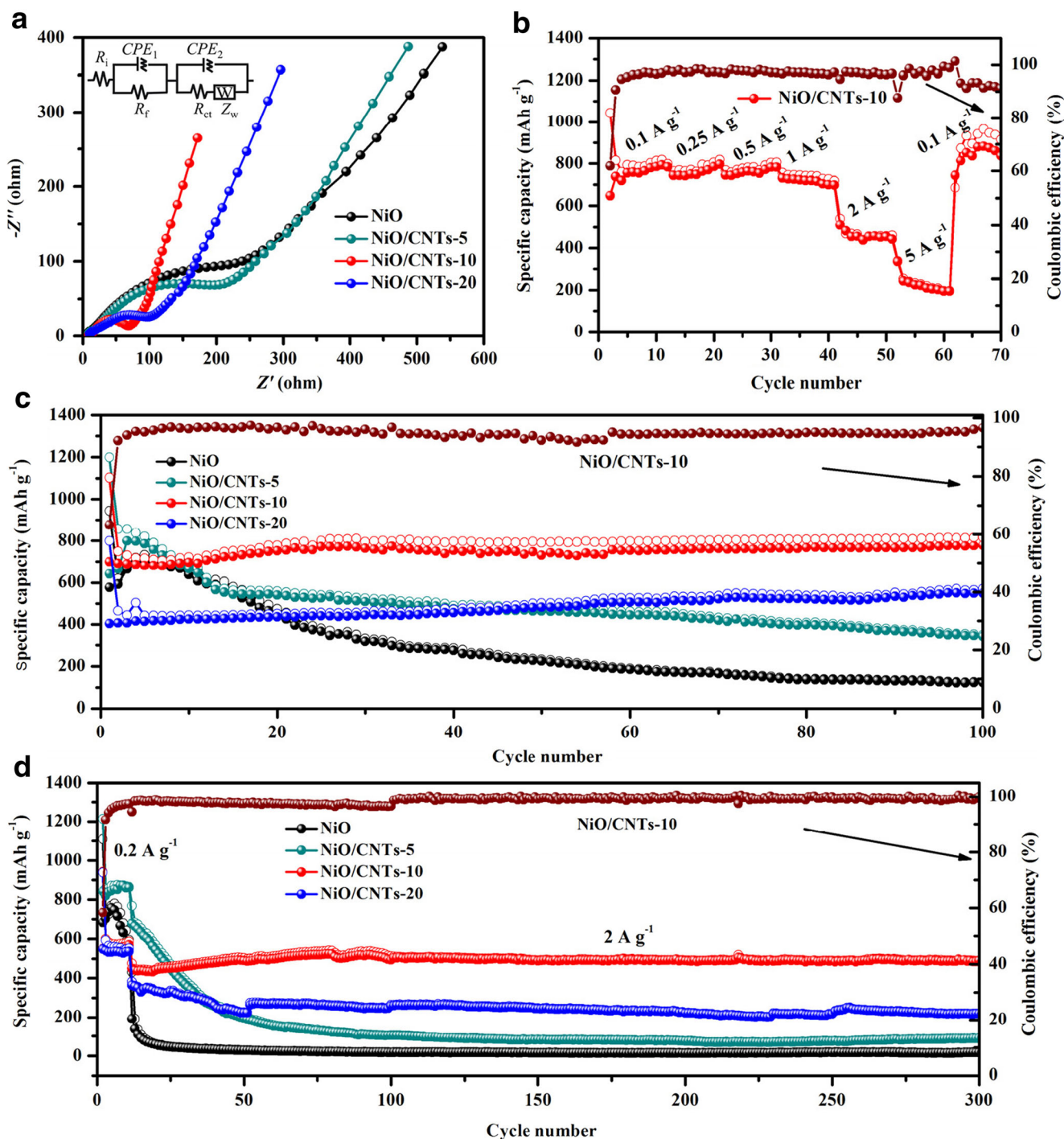
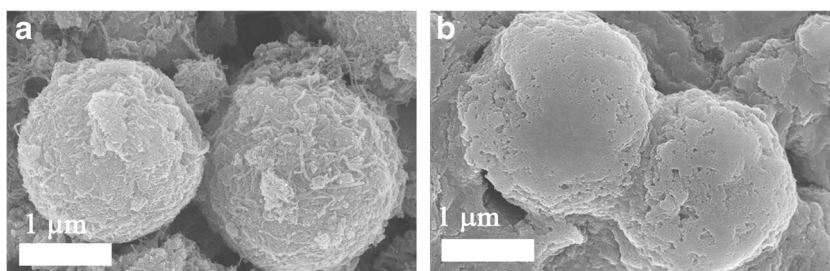


**Fig. 6** **a** EIS spectra of NiO and NiO/CNT composite electrodes after 100 charge-discharge cycles. The inset shows the equivalent circuit model. **b** Rate performance of NiO/CNTs-10. Cycling performances of NiO and NiO/CNTs at a current density of 100 mA g<sup>-1</sup> (**c**) and at a current density of 2 A g<sup>-1</sup> (**d**)

100 cycles, showing a poor capacity retention of 12.8%, which should result from the huge volume changes during cycling process and the poor electrical conductivity of NiO [26]. In contrast, all the NiO/CNT composites show better cycling performance and higher reversible capacity than NiO. In particular, the NiO/CNTs-10 delivers the highest reversible capacity of 812 mAh g<sup>-1</sup> after 100 cycles with a

coulombic efficiency of 96%, which is superior to those of other NiO-based electrode materials (as shown in Table S2). Even at 2 A g<sup>-1</sup> (Fig. 6d), NiO/CNT-10 also maintains a high reversible capacity of 502 mAh g<sup>-1</sup> after 300 cycles with good cycling stability. The excellent stability and high capacity of NiO/CNTs-10 should be ascribed to the following advantages: (a) the introduction of CNTs can alleviate the volume change

**Fig. 7** FESEM images of NiO/CNTs-10 electrode: **a** before and **b** after 100 cycles at a current density of  $100 \text{ mA g}^{-1}$



[50, 52] and increase the electrical conductivity of NiO [36] during cycling, resulting in excellent cycling performance; (b) the porous structure of microspheres assembled with nanoparticles should benefit to ion migration inside the microspheres; and (c) high specific surface area and the 3D network porous structure of NiO/CNTs-10 can enhance the electrode/electrolyte contact area and shorten the  $\text{Li}^+$  diffusion distance. However, excessive CNTs (NiO/CNTs-20) can reduce the capacity of NiO/CNTs owing to the poor electrochemical activity of CNTs. Therefore, a suitable amount of

CNTs (NiO/CNTs-10) is proposed for superior electrochemical performance. In order to further explore the improved structural stability of NiO/CNTs-10, the morphologies of electrode material before and after 100 cycles at  $100 \text{ mA g}^{-1}$  were characterized by FESEM, as shown in Fig. 7a, b. It can be found that NiO/CNTs-10 still maintains the microsphere structure of NiO after 100 cycles, implying the excellent cycling stability and good rate performance. However, the microspheres are covered with a thin SEI layer, resulting in their fuzzier surface. The FESEM image of NiO electrode is

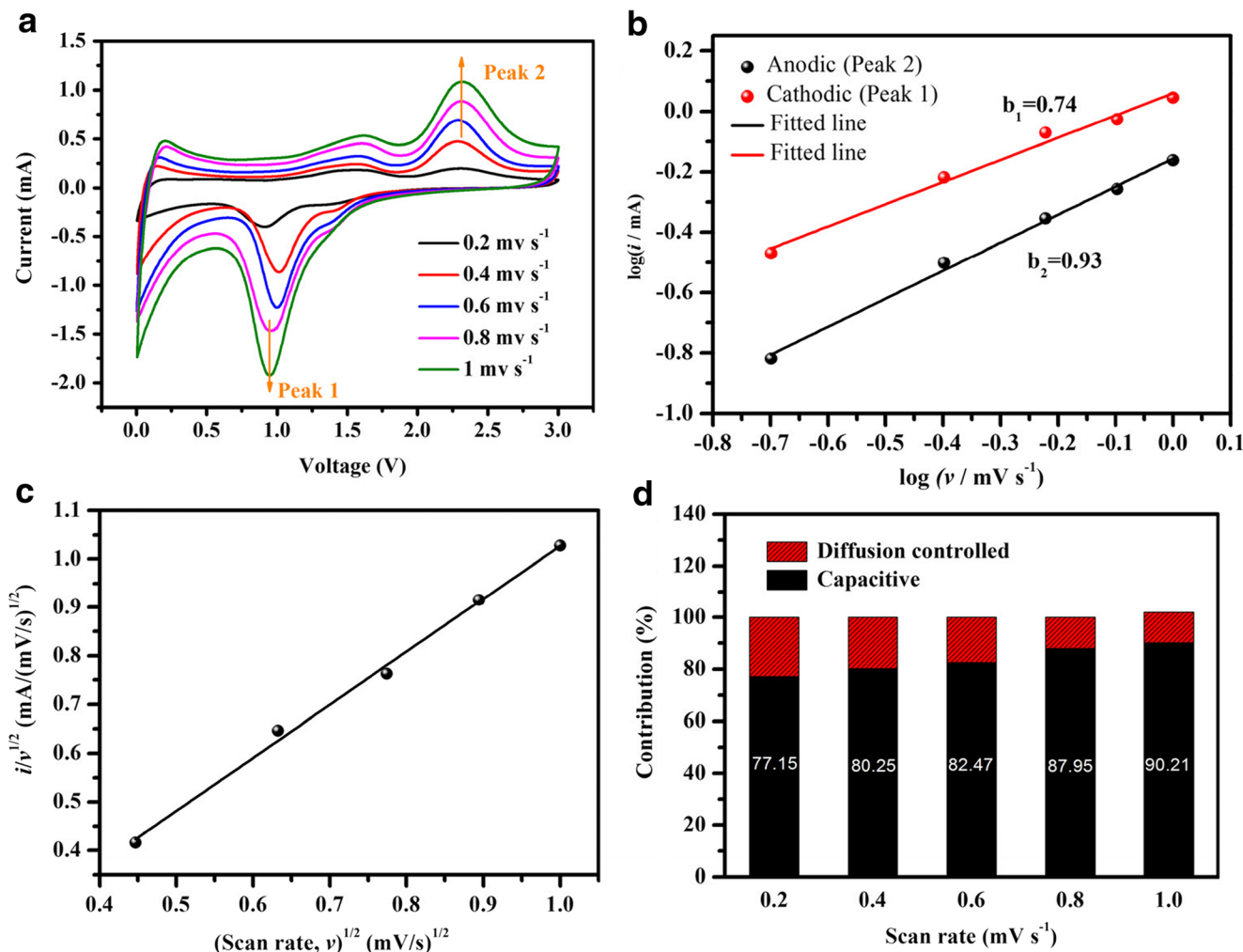


**Fig. 8** **a** CV curves of NiO/CNTs-10 at scan rates from 0.2 to  $1 \text{ mV s}^{-1}$ . **b** Linear relationships between  $\log i$  and  $\log v$ . **c** The fitting line of  $v^{1/2}$  versus  $i/v^{1/2}$  for anodic peak (2.3 V). **d** Contribution ratios of capacitive capacities at different scan rates



also characterized at the same condition. As shown in Fig. S3, almost of all NiO microspheres have been obviously agglomerated together and collapsed, indicating the fast capacity fading.

To further investigate the kinetic behavior during the lithium-ion storage process, CV tests of NiO/CNTs-10 with different scan rates (from 0.2 to 1 mV s<sup>-1</sup>) were carried out, as shown in Fig. 8a. On the basis of previous reports, lithium-ion storage behavior generally includes two components: diffusion-controlled contribution and capacitive effects [53]. According to the power-law relationship in Eq. (2) [54]:

$$i = av^b \quad (2)$$

where  $a$  and  $b$  are the parameters and the  $b$  value is determined by the slope of the  $\log v$  versus  $\log i$  plot. When the value of  $b$  is close to 0.5, the reaction is mainly controlled by a diffusion-controlled process, whereas  $b$  near to 1.0 represents that the system is dominated by capacitive effects [55, 56]. Figure 8b shows the plots of  $\log v$  versus  $\log i$  at oxidation (about 2.3 V) and reduction processes (about 0.9 V) of the CV curve. The  $b$  values are calculated to be 0.93 and 0.74 for the oxidation and reduction process, respectively, indicating that the lithium-ion storage of NiO/CNTs-10 mainly comes from capacitive behavior. In addition, we further quantified the capacitive contribution according to the Eq. (3) [53, 56]:

$$i = k_1v + k_2v^{1/2} \quad (3)$$

where  $k_1v$  and  $k_2v^{1/2}$  correspond to the current contributions from the capacitive effects and the diffusion-controlled process, respectively. Figure 8c shows that  $k_1$  is determined by the slope through plotting  $i/v^{1/2}$  versus  $v^{1/2}$ . Therefore, both capacitive and diffusion contributions are obtained, as shown in Fig. 8d. It is found that the capacitive contributions of NiO/CNTs-10 are 77.15, 80.25, 82.47, 87.95, and 90.21% as the scan rate increases from 0.2 to 1.0 mV s<sup>-1</sup>, showing that the capacitive capacity is improved with the increase of scan rate. This is indicating that NiO/CNTs-10 possesses an excellent cycling performance at high current density and superior rate capability.

## Conclusions

In summary, the NiO/CNT composites were successfully synthesized through thermal treatment Ni-MOFs/CNT precursor and their lithium-ion storage performances were evaluated. The results reveal that NiO/CNT composites exhibit excellent cycling stability and high specific capacity mainly due to the synergistic effect between NiO and CNTs as well as the 3D network porous structure. A maximum capacity of 812 mAh g<sup>-1</sup> after 100 cycles at 100 mA g<sup>-1</sup> is achieved for NiO/CNTs-10. Even at 2 A g<sup>-1</sup>, a capacity of 502 mAh g<sup>-1</sup> is

still kept after 300 cycles. The results show that NiO/CNT composites are attractive as potential anodes for LIBs.

**Acknowledgements** Financial support from the Basic Research Project of Shanghai Science and Technology Committee (NSSo. 14JC1491000), Key Project of National Natural Science Foundation of China (No. 61231003), and CAS Interdisciplinary Innovation Team is gratefully acknowledged.

## References

- Lu J, Chen ZH, Ma ZF, Pan F, Curtiss LA, Amine K (2010) The role of nanotechnology in the development of battery materials for electric vehicles. *Nat Nanotech* 11:1031–1038
- Hameer S, Niekerk JL (2015) A review of large-scale electrical energy storage. *Int J Energy Res* 39:1179–1195
- Peters JF, Baumann M, Zimmermann B, Braun J, Weil M (2017) The environmental impact of Li-ion batteries and the role of key parameters—a review. *Renew Sust Energ Rev* 67:491–506
- Guo BK, Wang XQ, Fulvio PF, Chi MF, Mahurin SM, Sun XG, Dai S (2011) Soft-templated mesoporous carbon-carbon nanotube composites for high performance lithium-ion batteries. *Adv Mater* 23:4661–4666
- Wu ZS, Zhou GM, Yin LC, Ren WC, Li F, Cheng HM (2012) Graphene/metal oxide composite electrode materials for energy storage. *Nano Energy* 1:107–131
- Li Q, Huang G, Yin DM, Wu YM, Wang LM (2016) Synthesis of porous NiO nanorods as high-performance anode materials for lithium-ion batteries. *Part Part Syst Charact* 33:764–770
- Mollamahale YB, Liu Z, Zhen YD, Tian ZQ, Hosseini D, Chen LW, Shen PK (2016) Simple fabrication of porous NiO nanoflowers: growth mechanism, shape evolution and their application into Li-ion batteries. *Int J Hydrog Energy* 42:7202–7211
- Zhang Z, Chu QX, Li HY, Hao JH, Yang WS, Lu BP, Ke X, Li J, Tang JL (2013) One-pot solvothermal synthesis of graphene-supported TiO<sub>2</sub> (B) nanosheets with enhanced lithium storage properties. *J Colloid Interface Sci* 409:38–42
- Chen FS, Liu XH, Zhang ZA, Zhang N, Pan AQ, Liang SQ, Ma RZ (2016) Controllable fabrication of urchin-like Co<sub>3</sub>O<sub>4</sub> hollow spheres for high-performance supercapacitors and lithium-ion batteries. *Dalton Trans* 45:15155–15161
- Zhao ZW, Wen T, Liang K, Jiang YF, Zhou X, Shen CC, Xu AW (2017) Carbon-coated Fe<sub>3</sub>O<sub>4</sub>/VO<sub>x</sub> hollow microboxes derived from metal-organic frameworks as a high-performance anode material for lithium-ion batteries. *ACS Appl Mater Interfaces* 9:3757–3765
- Jun Z, Chen JJ, Zhang CL, Qian H, Zheng MS, Dong QF (2014) The synthesis of a core-shell MnO<sub>2</sub>/3D-ordered hollow carbon sphere composite and its superior electrochemical capability for lithium ion batteries. *J Mater Chem A* 2:6343–6347
- Flügel EA, Ranft A, Haase F, Lotsch BV (2012) Synthetic routes toward MOF nanomorphologies. *J Mater Chem* 22:10119–10133
- Li SZ, Huo FW (2015) Metal-organic framework composites: from fundamentals to applications. *Nano* 7:7482–7501
- Wu RB, Qian XK, Zhou K, Wei J, Lou J, Ajayan PM (2014) Porous spinel Zn<sub>x</sub>Co<sub>3-x</sub>O<sub>4</sub> hollow polyhedra templated for high-rate lithium-ion batteries. *ACS Nano* 8:6297–6303
- Banerjee A, Aravindan V, Bhatnagar S, Mhamane D, Madhavi S, Ogale S (2013) Superior lithium storage properties of  $\alpha$ -Fe<sub>2</sub>O<sub>3</sub> nano-assembled spindles. *Nano Energy* 2:890–896
- Guo ZG, Cheng JK, Hu ZG, Zhang M, Xu Q, Kang ZX, Zhao D (2014) Metal-organic frameworks (MOFs) as precursors towards TiO<sub>x</sub>/C composites for photodegradation of organic dye. *RSC Adv* 4:34221–34225

17. DeKrafft KE, Wang C, Lin WB (2012) Metal-organic framework templated synthesis of Fe<sub>2</sub>O<sub>3</sub>/TiO<sub>2</sub> nanocomposite for hydrogen production. *Adv Mater* 24:2014–2018
18. Liu JJ, Yang Y, Zhu WW, Yi X, Dong ZL, Xu XN, Chen MW, Yang K, Lu G, Jiang LX, Liu Z (2016) Nanoscale metal-organic frameworks for combined photodynamic & radiation therapy in cancer treatment. *Biomaterials* 97:1–9
19. Meng WJ, Chen W, Zhao L, Huang Y, Zhu MS, Huang Y, Fu YQ, Geng FX, Yu J, Chen XF, Zhi CY (2014) Porous Fe<sub>3</sub>O<sub>4</sub>/carbon composite electrode material prepared from metal-organic framework template and effect of temperature on its capacitance. *Nano Energy* 8:133–140
20. Li GC, Liu PF, Liu R, Liu M, Tao K, Zhu SR, Wu MK, Yi FY, Han L (2016) MOF-derived hierarchical double-shelled NiO/ZnO hollow spheres for high-performance supercapacitors. *Dalton Trans* 45:13311–13316
21. Yue HY, Shi ZP, Wang QX, Cao ZX, Dong HY, Qiao Y, Yin YH, Yang ST (2014) MOF-derived cobalt-doped ZnO@C composites as a high-performance anode material for lithium-ion batteries. *ACS Appl Mater Interfaces* 6:17067–17074
22. Guo WX, Sun WW, Lv LP, Kong SF, Wang Y (2017) Microwave-assisted morphology evolution of Fe-based metal-organic frameworks and their derived Fe<sub>2</sub>O<sub>3</sub> nanostructures for Li-ion storage. *ACS Nano* 11:4198–4205
23. Wang BB, Wang G, Cheng XM, Wang H (2016) Synthesis and electrochemical investigation of core-shell ultrathin NiO nanosheets grown on hollow carbon microspheres composite for high performance lithium and sodium ion batteries. *Chem Eng J* 306:1193–1202
24. Xu X, Tan H, Xi K, Ding SJ, Yu DM, Cheng SD, Yang G, Peng XY, Fakeeh A, Kumar RV (2015) Bamboo-like amorphous carbon nanotubes clad in ultrathin nickel oxide nanosheets for lithium-ion battery electrodes with long cycle life. *Carbon* 84:491–499
25. Zou F, Chen YM, Liu KW, Yu ZT, Liang WF, Bhaway SM, Gao M, Zhu Y (2016) Metal organic frameworks derived hierarchical hollow NiO/Ni/graphene composites for lithium and sodium storage. *ACS Nano* 10:377–386
26. Zhang F, Jiang DG, Zhang XG (2016) Porous NiO materials prepared by solid-state thermolysis of a Ni-MOF crystal for lithium-ion battery anode. *Nano-Struct Nano-Objects* 5:1–6
27. Wu HJ, Wang YQ, Zheng CH, Zhu JM, Wu GL, Li XH (2016) Multi-shelled NiO hollow spheres: easy hydrothermal synthesis and lithium storage performances. *J Alloys Compd* 685:8–14
28. Jang JH, Chae BM, Oh HJ, Lee YK (2016) Understanding conversion mechanism of NiO anodic materials for Li-ion battery using in situ X-ray absorption near edge structure spectroscopy. *J Power Sources* 304:189–195
29. Fan XY, Li SH, Cui Y, Lu L, Zhou CF, Liu ZW (2016) Fe<sub>3</sub>O<sub>4</sub>/rice husk-based macro/mesoporous carbon bone nanocomposite as superior high-rate anode for lithium ion battery. *J Solid State Electrochem* 21:27–34
30. Luo SS, Xu S, Zhang YH, Liu JY, Wang SQ, He PX (2016) Preparation of MnO<sub>2</sub> and MnO<sub>2</sub>/carbon nanotubes nanocomposites with improved electrochemical performance for lithium ion batteries. *J Solid State Electrochem* 20:2045–2053
31. Brisbois M, Caes S, Sougrati MT, Vertruyen B, Schrijnemakers A, Cloots R, Eshraghi N, Hermann RP, Mahmoud A, Boschini F (2016) Na<sub>2</sub>FePO<sub>4</sub>F/multi-walled carbon nanotubes for lithium-ion batteries: Operando Mössbauer study of spray-dried composites. *Sol Energy Mater Sol Cells* 148:67–72
32. Cheng JL, Wang B, Park CM, Wu YP, Huang H, Nie FD (2013) CNT@Fe<sub>3</sub>O<sub>4</sub>@C coaxial nanocables: one-pot, additive-free synthesis and remarkable lithium storage behavior. *Chem Eur J* 19:9866–9874
33. Mahmoud A, Caes S, Brisbois M, Hermann RP, Berardo L, Schrijnemakers A, Malherbe C, Eppe G, Cloots R, Vertruyen B, Boschini V (2017) Spray-drying as a tool to disperse conductive carbon inside Na<sub>2</sub>FePO<sub>4</sub>F particles by addition of carbon black or carbon nanotubes to the precursor solution. *J Solid State Electrochem*. <https://doi.org/10.1007/s10008-017-3717-x>
34. Huang G, Zhang FF, Du XC, Qin YL, Yin DG, Wang LM (2015) Metal organic frameworks route to in situ insertion of multiwalled carbon nanotubes in Co<sub>3</sub>O<sub>4</sub> polyhedra as anode materials for lithium-ion batteries. *ACS Nano* 9:1592–1599
35. Zou YL, Qi ZG, Ma ZS, Jiang WJ, Hu RW, Duan JL (2017) MOF-derived porous ZnO/MWCNTs nanocomposite as anode materials for lithium-ion batteries. *J Electroanal Chem* 788:184–191
36. Abbas SM, Hussain ST, Ali S, Ahmad N, Ali N, Munawar KS (2013) Synthesis of carbon nanotubes anchored with mesoporous Co<sub>3</sub>O<sub>4</sub> nanoparticles as anode material for lithium-ion batteries. *Electrochim Acta* 105:481–488
37. Liu Y, Qiao Y, Zhang WX, Li Z, Hu XL, Yuan LX, Huang YH (2012) Coral-like α-MnS composites with N-doped carbon as anode materials for high-performance lithium-ion batteries. *J Mater Chem* 22:24026–24033
38. Xu XT, Wang M, Liu Y, Lu T, Pan LK (2016) Metal-organic framework-engaged formation of a hierarchical hybrid with carbon nanotube inserted porous carbon polyhedra for highly efficient capacitive deionization. *J Mater Chem A* 4:5467–5473
39. Pang HC, Guan BQ, Sun WW, Wang Y (2016) Metal-organic-frameworks derivation of mesoporous NiO nanorod for high-performance lithium ion batteries. *Electrochim Acta* 213:351–357
40. Chen TQ, Pan LK, Liu XJ, Sun Z (2013) A comparative study on electrochemical performances of the electrodes with different nanocarbon conductive additives for lithium ion batteries. *Mater Chem Phys* 142:345–349
41. Vogt C, Knowles GP, Chang SL, Chaffee AL (2013) Cadmium oxide/alkali metal halide mixtures—a potential high capacity sorbent for pre-combustion CO<sub>2</sub> capture. *J Mater Chem A* 1:10962–10971
42. Gou L, Liu PG, Liu D, Wang CY, Lei HY, Li ZY, Fan XY, Li DL (2017) Rational synthesis of Ni<sub>3</sub>(HCOO)<sub>6</sub>/CNT ellipsoids with enhanced lithium storage performance: inspired by the time evolution of the growth process of a nickel formate framework. *Dalton Trans* 46:6473–6482
43. Zhou G, Zhu J, Chen YJ, Mei L, Duan XC, Zhang GH, Chen LB, Wang TH, Lu BG (2014) Simple method for the preparation of highly porous ZnCo<sub>2</sub>O<sub>4</sub> nanotubes with enhanced electrochemical property for supercapacitor. *Electrochim Acta* 123:450–455
44. Li GD, Han RM, Xu XY, Ren MM (2016) Facile synthesis of Mn-doped hollow Fe<sub>2</sub>O<sub>3</sub> nanospheres coated with polypyrrole as anodes for high-performance lithium-ion batteries. *RSC Adv* 6:48199–48204
45. Cao W, Hu AP, Chen XH, Liu XH, Liu P, Tang QL, Zhao XS (2016) NiO hollow microspheres interconnected by carbon nanotubes as an anode for lithium ion batteries. *Electrochim Acta* 213:75–82
46. Liu WW, Lu CX, Wang XL, Liang K, Tay BK (2015) In situ fabrication of three-dimensional, ultrathin graphite/carbon nanotube/NiO composite as binder-free electrode for high-performance energy storage. *J Mater Chem A* 3:624–633
47. Xu LL, Lu BG (2016) 3D-frame structure NiO@CNTs for ultrafast charge slow discharge lithium ion batteries. *Electrochim Acta* 210:456–461
48. Sun XL, Yan CL, Chen Y, Si WP, Deng JW, Oswald S, Liu LF, Schmidt OG (2014) Three-dimensionally “curved” NiO nanomembranes as ultrahigh rate capability anodes for Li-ion batteries with long cycle lifetimes. *Adv Energy Mater* 4:1300912
49. Liang J, Hu H, Park H, Xiao CH, Ding SJ, Paik U, Lou XW (2015) Construction of hybrid bowl-like structures by anchoring NiO nanosheets on flat carbon hollow particles with enhanced lithium storage properties. *Energy Environ Sci* 8:1707–1711

50. Mao WF, Ai G, Dai YL, Fu YB, Ma Y, Shi SW, Soe R, Zhang XH, Qu DY, Tang ZY, Battaglia VS (2016) In-situ synthesis of  $\text{MnO}_2$ @CNT microsphere composites with enhanced electrochemical performances for lithium-ion batteries. *J Power Sources* 310: 54–60
51. Chen MH, Liu JL, Chao DL, Wang J, Yin JH, Lin JY, Fan HJ, Shen ZX (2014) Porous  $\alpha$ - $\text{Fe}_2\text{O}_3$  nanorods supported on carbon nanotubes-graphene foam as superior anode for lithium ion batteries. *Nano Energy* 9:364–372
52. Eshraghi N, Caes S, Mahmoud A, Cloots R, Vertruyen B, Boschini F (2017) Sodium vanadium (III) fluorophosphate/carbon nanotubes composite (NVPF/CNT) prepared by spray-drying: good electrochemical performance thanks to well-dispersed CNT network within NVPF particles. *Electrochim Acta* 228:319–324
53. Wang J, Polleux J, Lim J, Dunn B (2007) Pseudocapacitive contributions to electrochemical energy storage in  $\text{TiO}_2$  (anatase) nanoparticles. *J Phys Chem C* 111:14925–14931
54. Qi H, Cao LY, Li JY, Huang JF, Xu ZW, Cheng YY, Kong XG, Yanagisawa K (2016) High pseudocapacitance in  $\text{FeOOH}/\text{rGO}$  composites with superior performance for high rate anode in Li-ion battery. *ACS Appl Mater Interfaces* 8:35253–35263
55. Zhang J, Zhang W, He T, Amiin IS, Kou ZK, Li JN, Mu SC (2017) Smart reconstruction of dual-carbon decorated MnO for anode with high-capacity and ultralong-life lithium storage properties. *Carbon* 115:95–104
56. Zhu Y, Peng LL, Chen DH, Yu GH (2016) Intercalation pseudocapacitance in ultrathin  $\text{VOPO}_4$  nanosheets: toward high-rate alkali-ion-based electrochemical energy storage. *Nano Lett* 16:742–747